Effects of Polymer-Grafted Natural Nanocrystals on the Structure and Mechanical Properties of Poly(lactic acid): A Case of Cellulose Whisker-*graft*-Polycaprolactone

Ning Lin,[1,2,3] Guangjun Chen,[1,2,3] Jin Huang,[1,2,3,4] Alain Dufresne,[4] Peter R. Chang[5,6]

[1]*College of Chemical Engineering, Wuhan University of Technology, Wuhan 430070, China*
[2]*State Key Laboratory of Pulp and Paper Engineering, South China University of Technology, Guangzhou 510640, China*
[3]*Key Laboratory of Cellulose and Lignocellulosics Chemistry, Guangzhou Institute of Chemistry, Chinese Academy of Sciences, Guangzhou 510650, China*
[4]*Ecole Francaise de Papeterie et des Industries Graphiques, Institut National Polytechnique de Grenoble BP65, 38402 Saint-Martin d'Héres Cédex, France*
[5]*Saskatoon Research Centre, Agriculture and Agri-Food Canada, 107 Science Place, Saskatoon, SK, S7N 0X2, Canada*
[6]*Department of Agricultural and Bioresource Engineering, University of Saskatchewan, Saskatoon, SK, S7N 5A9, Canada*

Received 13 August 2008; accepted 21 February 2009
DOI 10.1002/app.30308
Published online 8 May 2009 in Wiley InterScience (www.interscience.wiley.com).

ABSTRACT: In this work, polysaccharide nanocrystals—rodlike cellulose whiskers (CWs)—were surface-grafted with polycaprolactone (PCL) via microwave-assisted ring-opening polymerization, and filaceous cellulose whisker-*graft*-polycaprolactone (CW-*g*-PCL) nanoparticles were produced. Moreover, the resultant nanoparticles were incorporated into poly(lactic acid) (PLA) as a matrix, and they showed superior function for enhancing the mechanical performance of PLA-based materials in comparison with platelet-like nanoparticles of starch nanocrystal-*graft*-PCL. The optimal loading level of CW-*g*-PCL was 8 wt %, and this resulted in simultaneous enhancements of the strength and elongation of approximately 1.9- and 10.7-fold, respectively, over those of the neat PLA material. In this case, the rigid CW nanoparticles contributed to the endurance of higher stress, whereas the grafted PCL chains improved the association between the PLA matrix and the CW-*g*-PCL filler and hence facilitated the transfer of stress to the rigid CW nanoparticles. Furthermore, such a fully biodegradable PLA-based nanocomposite shows great potential for environmentally friendly materials because of its high mechanical performance. © 2009 Wiley Periodicals, Inc. J Appl Polym Sci 113: 3417–3425, 2009

Key words: mechanical properties; nanocomposites

INTRODUCTION

Renewable biopolymers have found unique applications as matrices, nanofillers, or both in new green bionanocomposites.[1] Moreover, the acidic or alkaline hydrolysis of natural polysaccharides, such as cellulose,[2] chitin,[3] and starch,[4,5] can produce rigid nanocrystals with a uniform structure, and hence they can be ingredients of choice for bionanocomposites. Besides exhibiting a reinforcing function similar to that of inorganic nanoparticles,[6–8] polysaccharide nanocrystals are readily available and nontoxic, and they also contribute biodegradability, biocompatibility, high reactivity, and easy processability.[2] In particular, because of increasing concern about the nanosecurity of inorganic nanoparticles, such biocompatible and biodegradable polysaccharide nanocrystals have received additional attention for developing new nanocomposite materials. So far, cellulose and chitin whiskers as well as starch nanocrystals (StNs) have successfully reinforced many natural and synthetic materials,[2,6–22] including

Correspondence to: J. Huang (huangjin@iccas.ac.cn) or P. R. Chang (changp@agr.gc.ca).

Contract grant sponsor: National Natural Science Foundation of China; contract grant number: 50843031.
Contract grant sponsor: Société Francaise d'Exportation des Ressources Educatives.
Contract grant sponsor: Program of Energy Research and Development of Canada.
Contract grant sponsor: Agricultural Bioproducts Innovation Program of Canada via the Pulse Research Network.
Contract grant sponsor: Youth Chenguang Program of Science and Technology in Wuhan; contract grant number: 200850731383.
Contract grant sponsor: State Key Laboratory of Pulp and Paper Engineering, South China University of Technology; contract grant numbers: 200514, 200716.
Contract grant sponsor: Key Laboratory of Cellulose and Lignocellulosics Chemistry, Guangzhou Institute of Chemistry, Chinese Academy of Sciences; contract grant numbers: LCLC-2005-172, LCLC-2008-02.

poly(lactic acid) (PLA).[17,18] Even though the polar hydroxyl groups on natural nanocrystals could participate in the formation of covalent bonds and physical interactions[15] or self-associate as a network structure,[7] the weaker interfacial interaction between the polysaccharide nanocrystals and polymer matrix still inhibits the positive function of natural nanocrystals. Furthermore, the self-aggregation of polysaccharide nanocrystals results in a poor dispersion and then restricts the enhancement of the mechanical performances of nanocomposites. As a result, great efforts have been devoted to improving the interfacial adhesion and resultant compatibility between natural nanocrystals and polymeric matrices by surface chemical modification.[23–31] In this case, the reactive surface of polysaccharide nanocrystals played a key role in facilitating chemical derivation and grafting. When the chemically derived nanocrystals could not play the expected function, as mentioned previously,[7,25] the strategy of grafting long chains onto the surface of polysaccharide nanocrystals contributed to the transformation of polysaccharide nanocrystals into a cocontinuous material with high mechanical performance.[32] This concept was verified in our previous work. The polycaprolactone (PCL)-grafted starch and cellulose nanocrystals were incorporated into PCL,[32] PLA,[30] and waterborne polyurethane[33] as matrices, and this resulted in an increase in Young's modulus (E) and even simultaneous enhancements of the strength and elongation. In contrast with ungrafted nanocrystal-based nanocomposites, the materials processed from PCL-grafted nanocrystals displayed both a high modulus and good ductility.[32]

In this work, another polymer-grafted polysaccharide nanocrystal, cellulose whisker-*graft*-polycaprolactone (CW-*g*-PCL), was used to enhance the mechanical properties of a biomass material based on PLA. In particular, the rod structure of cellulose whiskers (CWs), which are distinctly different from platelet-like StNs, was expected to better enhance the strength and elongation simultaneously. Furthermore, good miscibility between the grafted PCL chains and PLA matrix[34,35] is an essential guarantee of improving the association between the CW-*g*-PCL nanofiller and PLA matrix. The composition and structure of the CW-*g*-PCL nanoparticles were characterized with elemental analysis, Fourier transform infrared (FTIR) spectroscopy, and transmission electron microscopy (TEM). Meanwhile, the structure and mechanical properties of the PLA/CW-*g*-PCL nanocomposites were investigated with X-ray diffraction (XRD), scanning electron microscopy (SEM), differential scanning calorimetry (DSC), dynamic mechanical analysis (DMA), and tensile testing. Finally, in comparison with the effects of the StN-*g*-PCL nanoparticles on the PLA-based materials, the role of the CW-*g*-PCL nanoparticles was realized.

EXPERIMENTAL

Materials

Commercial PLA pellets were purchased from Shenzhen Bright China Industry Co., Ltd. (Shenzhen, China), and the number-average molar weight and polydispersity were 8.1×10^4 and 1.80, respectively. The linter was kindly supplied by Hubei Chemical Fiber Group Co., Ltd. (Xiangfan, Hubei, China). ε-Caprolactone (CL) monomer was purchased from Alfa Aesar (Ward Hill, MA) and used as received. Tin(II) octoate [$Sn(Oct)_2$], sulfuric acid (H_2SO_4), and other analytical-grade reagents were purchased from Shanghai Sinopharm Chemical Co., Ltd. (Shanghai, China), and used as received.

Extraction and grafting of CWs

The CWs were prepared by H_2SO_4 hydrolysis of native linter. Linter (20 g) was dispersed into 175 mL of 30% (v/v) H_2SO_4 and then stirred with a stirring speed of 100 rpm for 6 h under 60°C. The resultant suspension was washed with distilled water by successive centrifugation until approximate neutrality was achieved. Subsequently, a small amount of ammonia (5 wt %) was added, and this was followed by dialysis with distilled water overnight. At last, the loose CW powder was obtained by lyophilization.

The preparation of CW-*g*-PCL via ring-opening polymerization under microwave irradiation can be described as follows. The CW powder was vacuum-dried at the ambient temperature (ca. 25°C) for 48 h before grafting polymerization to eliminate the interference of water. The CWs and CL monomer were placed into an ampule, in which the weight ratio of CWs to CL was 1 : 40. Subsequently, the $Sn(Oct)_2$ catalyst was added, and its weight was 0.5% of the CL weight. The mixture was homogenized with a Lab Dancer (IKA, Staufen, Germany) and then vacuum-exhausted for 30 min. Thereafter, the ampule containing the reactant was conditioned for 5 min under microwave irradiation with a power of 160 W. Subsequently, the crude product was dispersed by CH_2Cl_2 and then precipitated by methanol. This process of purification was carried out many times to remove the residual monomer and catalyst as well as the homopolymer.[30] During this purification process, the classification of deposition was carried out to remove the homopolymer because of a distinct difference in the molecular weights of the CW-*g*-PCL copolymer and the PCL homopolymer as well as the poor solubility of the CW component in CH_2Cl_2. Meanwhile, the initial precipitate was

collected during every step of purification, whereas FTIR spectroscopy was used to trace every precipitate until the relative intensity of the —C=O peak assigned to PCL was almost invariable. At last, the purified product, named CW-*g*-PCL, was vacuum-dried, and then it was kept in a desiccator containing silica gel for use.

Preparation of the PLA nanocomposites filled with CW-*g*-PCL

A desired amount of CW-*g*-PCL together with 2.0 g of PLA was mixed in CH_2Cl_2 under mechanical stirring to produce a mixture. Thereafter, the mixture was conditioned overnight to eliminate the bubbles and then cast into a Teflon mold; this was followed by evaporation of the solvent of CH_2Cl_2 at the ambient temperature (ca. 25°C) for 24 h. At last, the solidified films with a thickness of about 0.2 mm were vacuum-dried overnight, and they were then kept in the desiccator containing the silica gel. The resultant nanocomposite films were coded as PLA/CW-*g*-PCL(1), PLA/CW-*g*-PCL(4), PLA/CW-*g*-PCL(8), and PLA/CW-*g*-PCL(12); the Arabic numerals in parentheses represent the theoretical contents of CW-*g*-PCL in the nanocomposites. In addition, a neat PLA film was also prepared according to the aforementioned process without the addition of CW-*g*-PCL, and it was coded as PLA-F.

Characterization

FTIR spectra of the CW and CW-*g*-PCL powders as well as all the films were recoded on an FTIR 5700 spectrometer (Nicolet, Madison, WI). The powders were measured with a KBr-pellet method in the range of 4000–400 cm^{-1}, and the films were scanned in the range of 4000–700 cm^{-1} with Smart OMNT reflection accessories.

Elemental analysis of the CW-*g*-PCL and CW powders was carried out on a Vario EL III elemental analyzer (Elementar, Hanau, Germany).

XRD measurements were performed on a D/max-2500 X-ray diffractometer (Rigaku Denki, Tokyo, Japan) with Cu Kα_1 radiation (wavelength = 0.154 nm) in the 2θ range of 2–60° with a fixed time mode with a step interval of 0.02°.

TEM observations were carried out with an H-7000FA electron microscope (Hitachi, Tokyo, Japan) at 75 kV. A very small amount of the CW-*g*-PCL powder was dispersed in CH_2Cl_2 and then dispersed in distilled water; this was followed by rotating evaporation to remove CH_2Cl_2. At the same time, the CW powder was directly dispersed in distilled water. The aqueous CW and CW-*g*-PCL suspensions were diluted to a concentration of about 0.5 wt % and then negatively stained with a 2% (w/v) aqueous solution of uranyl acetate.

SEM observations were carried out with an X-650 scanning electron microscope (Hitachi, Tokyo, Japan). The films were frozen in liquid nitrogen and then snapped immediately. The fracture surfaces of the films were sputtered with gold and then observed and photographed.

DSC analysis was performed on a DSC-Q200 instrument (TA Instruments, New Castle, DE) under a nitrogen atmosphere at a heating or cooling rate of 20°C/min. The films were scanned in the range of −90 to 200°C after a pretreatment (heating from 20 to 100°C and then cooling to −90°C) for eliminating the thermal history.

DMA was performed on a DMA 242C dynamic mechanical analyzer (Netzsch, Hanau, Germany) with a dual cantilever device at a frequency of 1 Hz. The temperature ranged from −150 to 100°C with a heating rate of 3°C/min. The dimensions of the testing specimens (with a thickness of ca. 0.20 mm) was 30 mm × 10 mm.

The mechanical parameters, including the tensile strength (σ_b), elongation at break (ε_b), and Young's Modulus (E), of all the films were measured on a CMT6503 universal testing machine (SANS, Shenzhen, China) with a tensile rate of 10 mm/min according to ISO 527-3:1995(E). The testing films were cut into quadrate strips with a width of 10 mm, and the distance between testing marks was 40 mm. The tested strips were kept at 35% humidity for 7 days before the measurements. A mean value of three replicates of each film was taken. Because the elongation of some nanocomposite films was about 10.7-fold greater than that of the neat PLA-F film, the true value of σ_b ($\sigma_{b,true}$) was calculated as follows: $\sigma_{b,true} = F/S$, where S and F are the cross-section area and the stress at break. S was determined under the assumption that the total volume of the sample remained constant during the test so that $S = S_0L_0/L$, where S_0 and L_0 are the initial cross-section area and the initial marked testing length respectively while L is the tensile length at break.

RESULTS AND DISCUSSION

Composition and morphology of the PCL-grafted CWs

Figure 1 shows the FTIR spectra of the CW-*g*-PCL and CW powders. In comparison with the CW spectrum, there are two specific changes for CW-*g*-PCL, that is, the distinct peak located at 2945 cm^{-1} and the newly strong absorption centered at 1724 cm^{-1}. The former is associated with the methylene groups in the grafted PCL chains, and the latter is also assignable to the ester carbonyl of grafted PCL chains. This indicates that PCL became a component of

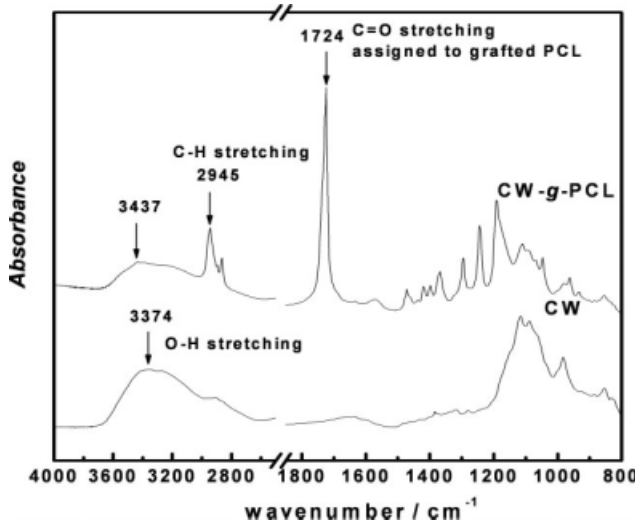

Figure 1 FTIR spectra of powders of CW-*g*-PCL nanoparticles and CWs as the reference.

CW-*g*-PCL. Furthermore, the absorption above 3000 cm^{-1}, assigned to O—H stretching of the CW component, decreased after the grafting of PCL. This suggests that the cellulose component existed in the grafted products. Because the purification mentioned in the Experimental section guaranteed the removal of the PCL homopolymer, FTIR verified that the PCL and CW components were successfully linked together to produce a new nanocomposite.

Although the exact number and length of grafted PCL chains were still difficult to determine with our great efforts, the PCL content could be calculated by elemental analysis. The contents of the C element in CW-*g*-PCL and CWs were determined to be 60.11 and 42.70%, respectively, whereas the theoretical content of the C element in PCL was 63.16%. Consequently, the content of grafted PCL chains in CW-*g*-PCL could be calculated with the following equation:

$$xC_{PCL} + (1 - x)C_{CW} = C_{CW-g-PCL}$$

where C_{PCL}, C_{CW}, and $C_{CW\text{-}g\text{-}PCL}$ are the contents of the C element in PCL, CWs, and CW-*g*-PCL, respectively, and x is the weight percentage of grafted PCL chains in CW-*g*-PCL. The result showed that the grafted PCL content was 85.09 wt %, which suggested that some PCL was located on the surface of CWs.

Just as in the previous report,[24,27] the ungrafted CWs showed a rodlike morphology. As shown in the TEM image in Figure 2(A), these rodlike nanoparticles could be seen to have a length of 200–300 nm and a diameter of 10–20 nm. However, after the grafting of PCL, the CW-*g*-PCL nanoparticles in the TEM image in Figure 2(B) showed a filaceous appearance with a length of several hundred nanometers. Obviously, these PCL-grafted nanocrystals had a certain degree of flexibility.

Mechanical properties of the PLA/CW-*g*-PCL nanocomposites

The resultant CW-*g*-PCL nanoparticles were incorporated into the PLA matrix to produce a kind of nanocomposite with better mechanical performance. Figure 3 shows the effects of the CW-*g*-PCL content on the mechanical parameters of the PLA/CW-*g*-PCL films, including $\sigma_{b,true}$, E, and ε_b. Here, $\sigma_{b,true}$ was used because the elongation of some nanocomposite films was greater than that of the PLA-F film. With an increase in the CW-*g*-PCL content, $\sigma_{b,true}$ of the PLA/CW-*g*-PCL nanocomposite films increased until the loading level of 8 wt %, and then it decreased. In this case, $\sigma_{b,true}$ of the PLA/CW-*g*-PCL(8) nanocomposite reached a maximum value of 75.5 MPa, which was enhanced by 85.5% in contrast with $\sigma_{b,true}$ of the PLA-F film (40.7 MPa). Despite the lower $\sigma_{b,true}$ value of the PLA/CW-*g*-PCL nanocomposite containing less than 4 wt % CW-*g*-PCL in contrast with the neat PLA-F, all the PLA/CW-*g*-PCL nanocomposite films showed dramatically increased ε_b values. The effect of the CW-*g*-PCL content on ε_b

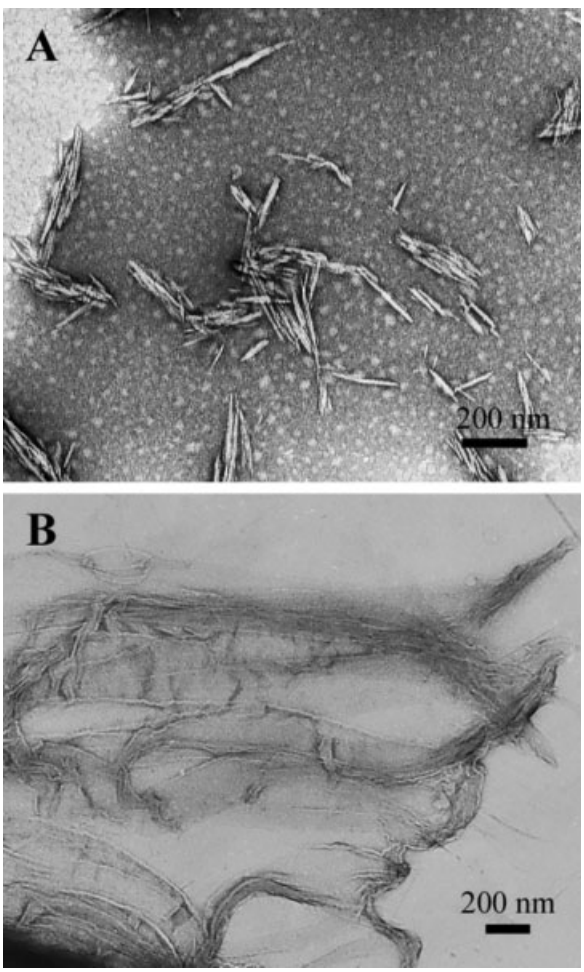

Figure 2 TEM images of (A) unmodified CW and (B) CW-*g*-PCL nanoparticles.

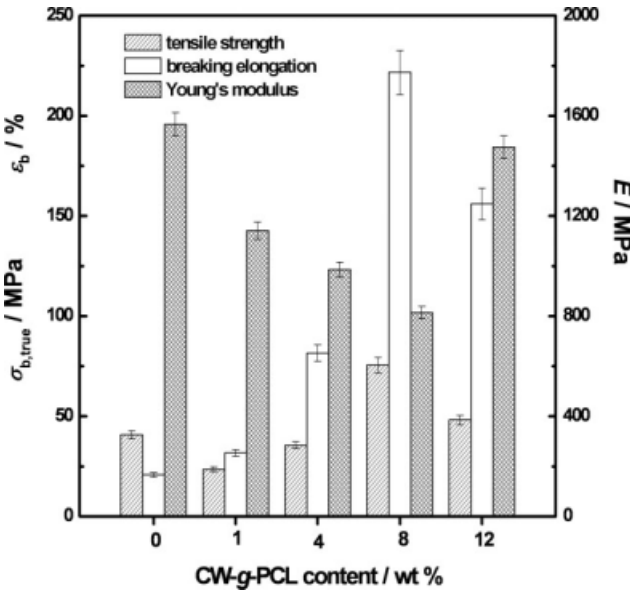

Figure 3 Effects of the CW-*g*-PCL content on σ_b, ε_b, and *E* for PLA/CW-*g*-PCL nanocomposite films containing various CW-*g*-PCL contents as well as the PLA-F film.

was similar to that on $\sigma_{b,true}$, and the PLA/CW-*g*-PCL(8) nanocomposite had a maximum ε_b value of 221.6%, which was 10.7-fold greater than that of the neat PLA-F. Meanwhile, the dependence of *E* on the CW-*g*-PCL content was just the opposite of that of ε_b. Consequently, the introduction of CW-*g*-PCL led to simultaneous enhancements of the strength and elongation of the PLA-based materials, and the optimal loading level of 8 wt % yielded the highest strength and elongation. Furthermore, the prominent enhancement of the elongation as well as the reduction of the modulus, due to the addition of CW-*g*-PCL, could contribute to extending the applications of PLA-based plastics.

Attenuated total reflectance/Fourier transform infrared (ATR–FTIR) spectra of the PLA/CW-*g*-PCL nanocomposites

The ATR–FTIR spectra of the PLA/CW-*g*-PCL nanocomposite films as well as the PLA-F film are shown in Figure 4. As expected, with an increase in the CW-*g*-PCL content, the absorption assigned to CW-*g*-PCL, such as the peak located at 1724 cm^{-1}, gradually became stronger. Furthermore, the relative intensities of the carbonyl absorption located at 1757 cm^{-1} for the PLA matrix decreased, in contrast to the increasing intensities of carbonyl absorption located at 1724 cm^{-1}, which was assigned to the PCL component. If the CW-*g*-PCL filler and PLA matrix were absolutely separated, the increase in the peak intensities located at 1724 cm^{-1} should be proportional to the increase in the CW-*g*-PCL content. However, with an increase in the CW-*g*-PCL content, the increasing extent of peak intensities located at 1724 cm^{-1} gradually decreased, and this indicated that complexation existed between the PLA matrix and the CW-*g*-PCL filler.

XRD patterns of the PLA/CW-*g*-PCL nanocomposites

The XRD patterns of the PLA/CW-*g*-PCL nanocomposite films as well as the PLA-F film and the CW-*g*-PCL powder are shown in Figure 5. Because of the low content (<12 wt %) and weak diffraction of the CW component as well as the dominant crystallinity of the PCL component, the CW-*g*-PCL powder showed only the distinct crystalline character assigned to the PCL component, that is, two spiculate peaks located at 21.2 and 23.6° (2θ). Meanwhile, the XRD pattern of the PLA-F film showed a semicrystalline character. There were three weak diffractions located at 9.5, 28.7, and 29.4° (2θ) as well as one diffuse peak located around 17.2° (2θ). The PLA/CW-*g*-PCL nanocomposite with the lowest

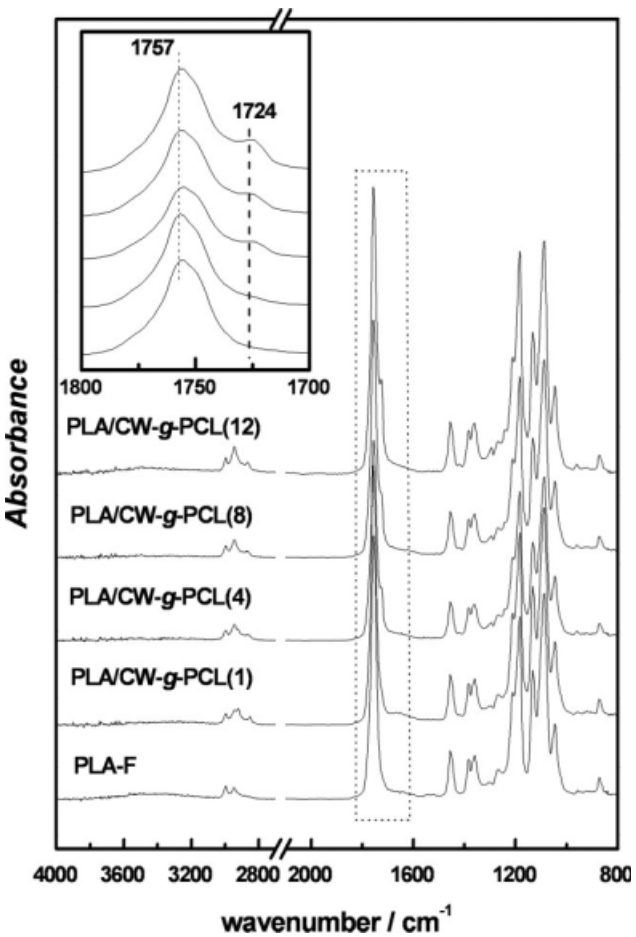

Figure 4 Full ATR–FTIR spectra and a magnification of the range of 1800–1700 cm^{-1} for PLA/CW-*g*-PCL nanocomposite films containing various CW-*g*-PCL contents as well as the PLA-F film.

loading level of 1 wt % CW-*g*-PCL showed a diffraction pattern similar to that of PLA-F. This suggested that CW-*g*-PCL could dissolve into the PLA matrix because of the good miscibility between PCL and PLA.[34,35] However, with an increase in the CW-*g*-PCL content, a distinct diffraction peak located at 16.7° (2θ) appeared in the diffuse diffraction. It might have resulted from the formation of a new crystalline form induced by the nucleation of CW-*g*-PCL. When the CW-*g*-PCL loading level reached 12 wt %, all the small diffraction peaks disappeared for PLA/CW-*g*-PCL(12). This suggested that the original structure of the PLA matrix was cleaved to a greater extent.

Thermal properties of the PLA/CW-*g*-PCL nanocomposites

DSC and DMA were used to further understand the interaction between the CW-*g*-PCL filler and the PLA matrix as well as the structural changes in the PLA/CW-*g*-PCL nanocomposites through the observation of the variances of the domain-scale glass transition and molecular-level α relaxation assigned to the PLA matrix as well as the melting transitions of the grafted PCL chains and the PLA matrix, respectively. DSC thermograms of the PLA/CW-*g*-PCL nanocomposites as well as PLA-F are depicted in Figure 6, and detailed data, such as the glass-transition temperature at the midpoint ($T_{g,\mathrm{mid}}$) and heat-capacity increment (ΔC_p) assigned to the PLA matrix as well as the melting temperature (T_m) and heat enthalpy (ΔH_m) assigned to the PCL component and PLA matrix, are summarized in Table I. The glass transition of grafted PCL chains was not observed, and therefore CW-*g*-PCL showed only a melting transition of double peaks assigned to the grafted PCL chains, which were located at 46.2 and 51.4°C. Together with the predominant crystalline diffraction in the XRD pattern of Figure 5, the grafted PCL chains were mainly in a crystalline form. However, the value of $T_{m,\mathrm{PCL}}$ assigned to CW-*g*-PCL in the PLA/CW-*g*-PCL nanocomposites increased up to about 70°C. This resulted from the restriction of the glassy amorphous region and the crystalline domains in the PLA matrix. Furthermore, with an increase in the CW-*g*-PCL content, the $\Delta H_{m,\mathrm{PCL}}$ values gradually increased despite the analogous $T_{m,\mathrm{PCL}}$ values. Meanwhile, the neat PLA-F showed a glass transition with a $T_{g,\mathrm{mid}}$ value of 57.7°C and a melting transition with a $T_{m,\mathrm{PLA}}$ value of 147.7°C. However, the introduction of CW-*g*-PCL resulted in a shift of the $T_{g,\mathrm{mid}}$ values assigned to the PLA matrix for the PLA/CW-*g*-PCL nanocomposites down to about 52°C. This suggested that the motion of PLA

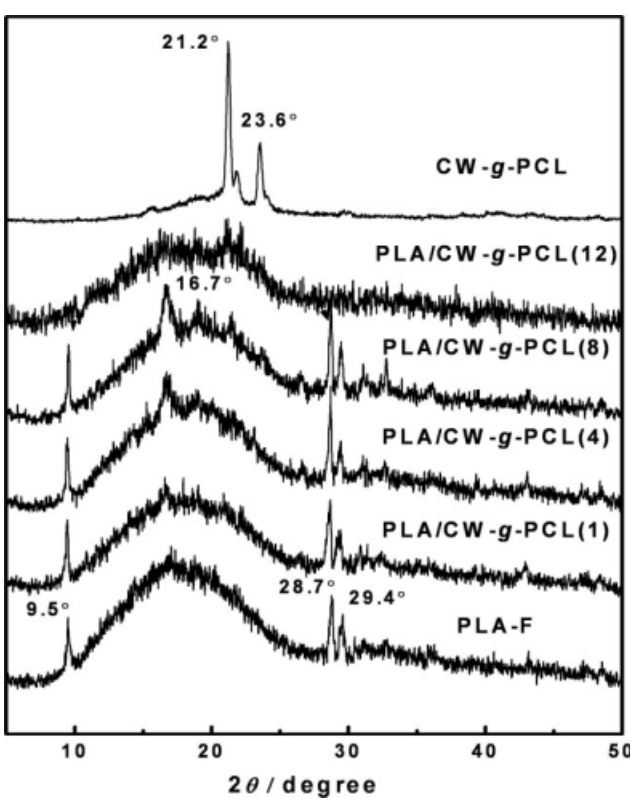

Figure 5 XRD patterns of PLA/CW-*g*-PCL nanocomposites films containing various CW-*g*-PCL contents as well as the PLA-F film and CW-*g*-PCL nanoparticles.

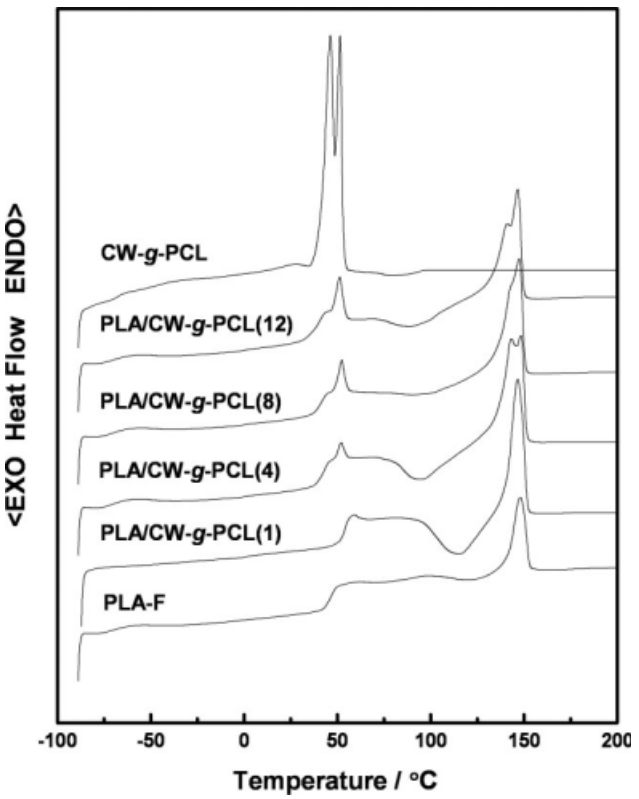

Figure 6 DSC thermograms of PLA/CW-*g*-PCL nanocomposites films containing various CW-*g*-PCL contents as well as the PLA-F film.

TABLE I
DSC and DMA Data for the PLA/CW-*g*-PCL Nanocomposite Films as Well as the PLA-F Film and CW-*g*-PCL Powder

	DSC data						DMA data			
	PCL component		PLA matrix				Log E'-temperature curve		Tan δ-temperature curve	
Sample code	$T_{m,PCL}$ (°C)	$\Delta H_{m,PCL}$ (J/g)	$T_{g,mid}$ (°C)	ΔC_p (J g^{-1} K^{-1})	$T_{m,PLA}$ (°C)	$\Delta H_{m,PLA}$ (J/g)	$T_{\alpha,onset}$ (°C)	log E'_{onset} (MPa)	$T_{\alpha,max}$ (°C)	$H_{loss\text{-}peak}$
PLA-F	—	—	57.7	0.48	147.7	11.62	46.6	5.32	59.6	0.50
PLA/CW-*g*-PCL(1)	69.3	0.45	52.2	0.43	146.3	30.79	46.6	4.67	58.6	0.80
PLA/CW-*g*-PCL(4)	70.4	1.01	52.0	0.36	142.9/148.2[a]	29.44	37.6	4.38	54.6	0.57
PLA/CW-*g*-PCL(8)	70.0	2.18	52.4	0.30	142.8/147.3[a]	28.77	38.6	4.44	55.6	0.66
PLA/CW-*g*-PCL(12)	70.4	2.73	51.4	0.42	140.6/146.5[a]	23.93	35.6	4.47	53.6	0.64
CW-*g*-PCL	46.2/51.4[a]	52.69	—	—	—	—	—	—	—	—

E' = storage modulus; E'_{onset} = onset storage modulus; tan δ = loss factor; $H_{loss\text{-}peak}$ = height of loss-peak.
[a] The melting transitions assigned to the PCL component and the PLA matrix were divided into two fractions.

segments in the amorphous region was improved by the occurrence of the rubbery PCL component. At the same time, except for the melting transition of PLA/CW-*g*-PCL(1) with the lowest loading level of CW-*g*-PCL (similar to neat PLA-F), the melting peaks of the other PLA/CW-*g*-PCL nanocomposites containing more than 4 wt % CW-*g*-PCL were divided into two fractions. The one melting peak was located at a lower temperature of 140–143°C, and the other melting peak was close to $T_{m,PLA}$ of PLA-F. This indicated that the original structure (i.e., the size of the crystalline domains) of the PLA matrix was changed by the complexation between PLA and CW-*g*-PCL. In addition, the $\Delta H_{m,PLA}$ values of all the PLA/CW-*g*-PCL nanocomposites were dramatically higher than that of the neat PLA-F. This was attributed to the nucleation function of CW-*g*-PCL for improving the crystallinity of the PLA matrix.

DMA can be used to further determine the motion of the segments at a molecular level in contrast to the domain scale reflected by DSC. Curves of the logarithm of the storage modulus versus the temperature and the loss factor versus the temperature are shown in Figure 7, and the data associated with α relaxation (corresponding to the glass transition) are also summarized in Table I. Just like the DSC results, the α relaxation of the PCL component was still absent. Meanwhile, the improvement of the motion for the PLA segments was verified by the decreasing values of $T_{\alpha,onset}$ (i.e. a relaxation temperature at onset from log E'-T curve) and $T_{\alpha,max}$ (i.e. a relaxation temperature at loss peak from tan σ-T curve). However, $T_{\alpha,onset}$ and $T_{\alpha,max}$ of PLA/CW-*g*-PCL(1) were close to those of the neat PLA-F. This suggested that the chemical environment for the motion of the PLA segments experienced no obvious change due to the lowest loading level of CW-*g*-PCL. In addition, the PCL component in the rubbery state resulted in a lower storage modulus (i.e., logarithm of the onset storage modulus) for the nanocomposites, in contrast to the neat PLA-F.

Fractured morphologies of the PLA/CW-*g*-PCL nanocomposites

Figure 8 shows SEM images of the fractured morphologies of the PLA/CW-*g*-PCL nanocomposite

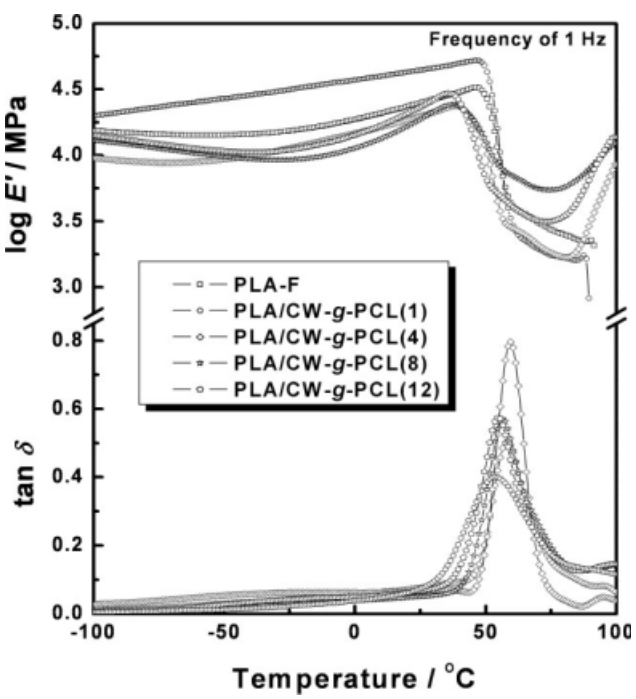

Figure 7 Logarithm storage modulus (log E') and loss factor (tan δ) as functions of temperature for PLA/CW-*g*-PCL nanocomposites films containing various CW-*g*-PCL contents as well as the PLA-F film.

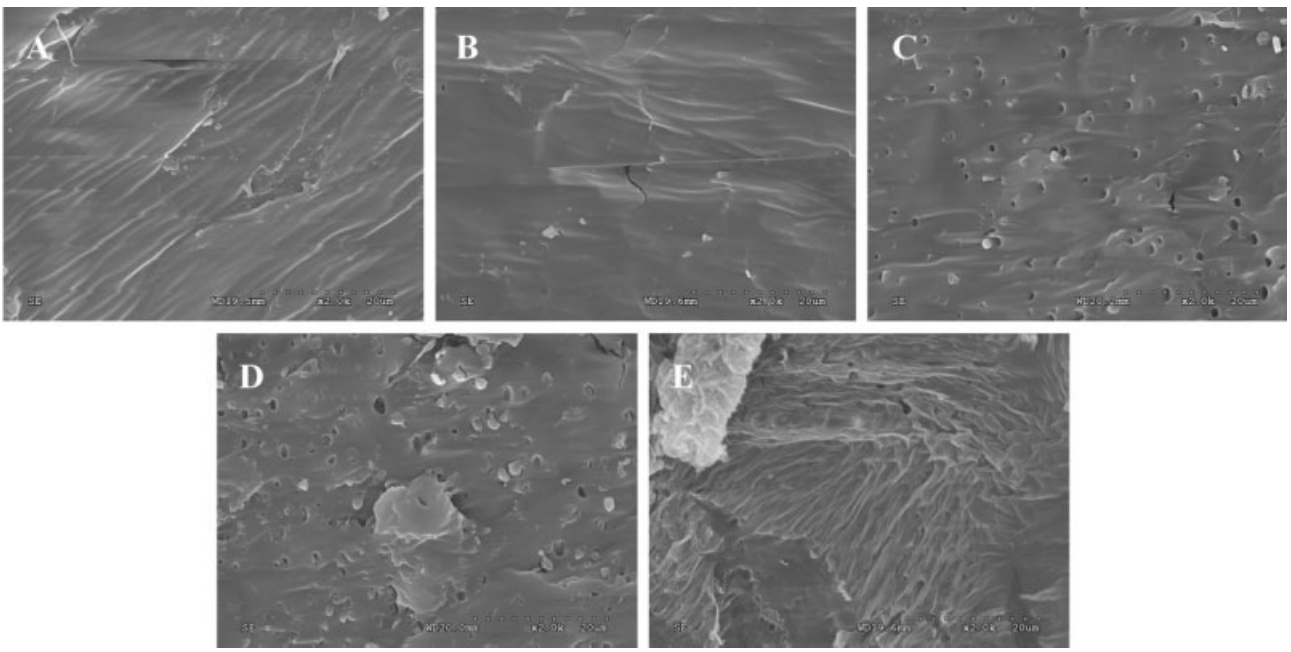

Figure 8 SEM images of fracture morphologies of PLA/CW-*g*-PCL nanocomposite films containing various CW-*g*-PCL contents and PLA-F: (A) PLA-F, (B) PLA/CW-*g*-PCL(1), (C) PLA/CW-*g*-PCL(4), (D) PLA/CW-*g*-PCL(8), and (E) PLA/CW-*g*-PCL(12).

films and the neat PLA-F film. Except for PLA/CW-*g*-PCL(1) with the lowest CW-*g*-PCL loading level, the fractured morphologies of the PLA/CW-*g*-PCL nanocomposite films were distinctly different from the striation-like fractured surface of the PLA-F film. PLA/CW-*g*-PCL(1) showed analogous striation on the fractured surface because the lowest loading level of CW-*g*-PCL could uniformly dissolve into the PLA matrix. However, when the CW-*g*-PCL content was increased up to 4 wt %, many small microparticles dispersed onto a porous plane. These pores resulted from the removal of microparticles. With a continuous increase in the CW-*g*-PCL content, the number of dispersed microparticles increased, whereas the fractured surface gradually became coarser. These microparticles might be assigned to the aggregates of CW-*g*-PCL and dispersed as rubbery fillers containing rigid CWs into the PLA matrix. Meanwhile, the original structure of the PLA matrix was also obviously changed.

Role of the CW-*g*-PCL nanofiller in the nanocomposites

It was previously verified that incorporating the PCL component into the PLA matrix would result in an increase in the elongation and decreases in the strength and *E*.[36] As a result, the increase in strength for the PLA/CW-*g*-PCL nanocomposites was mainly attributed to the stronger ability of the rigid CW nanoparticles to endure stress. Meanwhile, good miscibility between the grafted PCL chains and the PLA matrix[34,35] confirmed the essential associations for a facile transfer of the stress to the rigid CW nanoparticles. On the other hand, the grafted PCL component in a rubbery state provided higher flexibility to the PLA/CW-*g*-PCL nanocomposites for an increase in the elongation. In our previous work,[30] platelet-like StN-*g*-PCL was incorporated into the PLA matrix, and this resulted in simultaneous enhancements of the strength and elongation at an StN-*g*-PCL loading level of 5 wt %. In this case, CW-*g*-PCL showed a distinct morphology different from that of StN-*g*-PCL, that is, a flexible filaceous structure with a high length/diameter ratio. When the loading level of CW-*g*-PCL was 8 wt %, the strength and elongation of the PLA/CW-*g*-PCL nanocomposite were also enhanced at the same time. Furthermore, both the strength and elongation of PLA/CW-*g*-PCL(8) were higher than those of PLA/StN-*g*-PCL containing 5 wt % StN-*g*-PCL in the previous report.[30] It is pitiful that the PLA/CW-*g*-PCL nanocomposites with a loading level lower than 4 wt % had lower strength than neat PLA-F despite an increase in the elongation. However, PLA/CW-*g*-PCL(12) still showed simultaneous enhancements of the strength and elongation; in contrast, the PLA/StN-*g*-PCL nanocomposites had decreased strength when the StN-*g*-PCL content was higher than 10 wt %. In conclusion, filaceous CW-*g*-PCL had superior function for enhancing the mechanical properties of the PLA-based materials.

CONCLUSIONS

CW-*g*-PCL, a kind of polymer-grafted polysaccharide nanocrystal, was incorporated into a PLA matrix to produce new nanocomposite materials with high mechanical performance. When the loading level of CW-*g*-PCL was 8 wt %, $\sigma_{b,\text{true}}$ was enhanced by 85.5% in comparison with the PLA-F film, whereas the elongation was 10.7-fold greater than that of PLA-F. The simultaneous enhancements of the strength and elongation were attributed to the ability of rigid CW nanoparticles to endure higher stress as well as the essential associations of the facile transfer of the stress to the CW nanoparticles mediated with grafted PCL chains. Furthermore, the prominent enhancement of the elongation and the reduction of the modulus, due to the rubbery PCL component, might contribute to the application of PLA-based plastics. With respect to the mechanical properties of the PLA/StN-*g*-PCL nanocomposites, filaceous CW-*g*-PCL had superior function for enhancing the mechanical performance of PLA-based materials.

References

1. Darder, M.; Aranda, P.; Hitzky, R. E. Adv Mater 2007, 19, 1309.
2. Azizi Samir, M. A. S.; Alloin, F.; Dufresne, A. Biomacromolecules 2005, 6, 612.
3. Angellier, H.; Choisnard, L.; Molina-Boisseau, S.; Ozil, P.; Dufresne, A. Biomacromolecules 2004, 5, 1545.
4. Putaux, J.-L.; Molina-Boisseau, S.; Momaur, T.; Dufresne, A. Biomacromolecules 2003, 4, 1198.
5. Paillet, M.; Dufresne, A. Macromolecules 2001, 34, 6527.
6. Angellier, H.; Molina-Boisseau, S.; Dole, P.; Dufresne, A. Biomacromolecules 2006, 7, 531.
7. Angellier, H.; Molina-Boisseau, S.; Dufresne, A. Macromolecules 2005, 38, 9161.
8. Ljungberg, N.; Cavaillé, J. Y.; Heux, L. Polymer 2006, 47, 6285.
9. Chazeau, L.; Cavaillé, J. Y.; Canova, G.; Dendievel, R.; Boutherin, B. J Appl Polym Sci 1999, 71, 1797.
10. Garcia de Rodriguez, N. L.; Thielemans, W.; Dufresne, A. Cellulose 2006, 13, 261.
11. Chauve, G.; Heux, L.; Arouini, R.; Mazeau, K. Biomacromolecules 2005, 6, 2025.
12. Helbert, W.; Cavaillé, J. Y.; Dufresne, A. Polym Compos 1996, 17, 604.
13. Matos Ruiz, M.; Cavaillé, J. Y.; Dufresne, A, Graillat, C.; Gerard, J. F. Macromol Symp 2001, 169, 211.
14. Cavaillé, J. Y.; Dufresne, A.; Paillet, M.; Azizi Samir, M. A. S.; Alloin, F.; Sanchez, J. Y. Fr. Pat. FR2841255 (2002).
15. Chen, G.; Wei, M.; Chen, J.; Huang, J.; Dufresne, A.; Chang, P. R. Polymer 2008, 49, 1860.
16. Dufresne, A.; Kellerhals, M. B.; Witholt, B. Macromolecules 1999, 32, 7396.
17. Kvien, I.; Tanem, B. S.; Oksman, K. Biomacromolecules 2005, 6, 3160.
18. Petersson, L.; Kvien, I.; Oksman, K. Compos Sci Technol 2007, 67, 2535.
19. Morin, A.; Dufresne, A. Macromolecules 2002, 35, 2190.
20. Noshiki, Y.; Nishiyama, Y.; Wada, M.; Kuga, S.; Magoshi, J. J Appl Polym Sci 2002, 86, 3425.
21. Lu, Y.; Weng, L.; Cao, X. Carbohydr Polym 2006, 63, 198.
22. Zheng, H.; Ai, F.; Chang, P. R.; Huang, J.; Dufresne, A. Polym Compos 2009, 30, 474.
23. Dong, S.; Roman, M. J Am Chem Soc 2007, 129, 13810.
24. Yuan, H.; Nishiyama, Y.; Wada, M.; Kuga, S. Biomacromolecules 2006, 7, 696.
25. Nair, K. G.; Dufresne, A. Biomacromolecules 2003, 4, 1835.
26. Angellier, H.; Molina-Boisseau, S.; Belgacem, M. N.; Dufresne, A. Langmuir 2005, 21, 2425.
27. Araki, J.; Wada, M.; Kuga, S. Langmuir 2001, 17, 21.
28. Thielemans, W.; Belgacem, M. N.; Dufresne, A. Langmuir 2006, 22, 4804.
29. Labet, M.; Thielemans, W.; Dufresne, A. Biomacromolecules 2007, 8, 2916.
30. Yu, J.; Ai, F.; Dufresne, A.; Gao, S.; Huang, J.; Chang, P. R. Macromol Mater Eng 2008, 293, 763.
31. Song, S.; Wang, C.; Pan, Z.; Wang, X. J Appl Polym Sci 2008, 107, 418.
32. Habibi, Y.; Dufresne, A. Biomacromolecules 2008, 9, 1974.
33. Chang, P. R.; Ai, F.; Chen, Y.; Dufresne, A.; Huang, J. J Appl Polym Sci 2009, 111, 619.
34. Domb, A. J. J Polym Sci Part A: Polym Chem 1993, 31, 1973.
35. Sivalingam, G.; Vijayalakshmi, S. P.; Madras, G. Ind Eng Chem Res 2004, 43, 7702.
36. López-Rodríguez, N.; López-Arraiza, A.; Meaurio, E.; Sarasua, J. R. Polym Eng Sci 2006, 46, 1299.